Commun. Comput. Phys.
doi: 10.4208/cicp.2009.09.088

Vol. **7**, No. 5, pp. 1027-1048
May 2010

A Weighted Runge-Kutta Method with Weak Numerical Dispersion for Solving Wave Equations

Shan Chen, Dinghui Yang* and Xiaoying Deng

Department of Mathematical Sciences, Tsinghua University, Beijing 100084, China.

Received 21 May 2009; Accepted (in revised version) 17 November 2009

Communicated by Lianjie Huang

Available online 6 January 2010

Abstract. In this paper, we propose a weighted Runge-Kutta (WRK) method to solve the 2D acoustic and elastic wave equations. This method successfully suppresses the numerical dispersion resulted from discretizing the wave equations. In this method, the partial differential wave equation is first transformed into a system of ordinary differential equations (ODEs), then a third-order Runge-Kutta method is proposed to solve the ODEs. Like the conventional third-order RK scheme, this new method includes three stages. By introducing a weight to estimate the displacement and its gradients in every stage, we obtain a weighted RK (WRK) method. In this paper, we investigate the theoretical properties of the WRK method, including the stability criteria, numerical error, and the numerical dispersion in solving the 1D and 2D scalar wave equations. We also compare it against other methods such as the high-order compact or so-called Lax-Wendroff correction (LWC) and the staggered-grid schemes. To validate the efficiency and accuracy of the method, we simulate wave fields in the 2D homogeneous transversely isotropic and heterogeneous isotropic media. We conclude that the WRK method can effectively suppress numerical dispersions and source noises caused in using coarse grids and can further improve the original RK method in terms of the numerical dispersion and stability condition.

AMS subject classifications: 65M06, 65M12, 86-08, 86A15

Key words: WRK method, seismic wavefield modeling, anisotropy, numerical dispersion.

1 Introduction

Finite difference (FD) is the most widely used numerical scheme in solving the wave equation for wave propagation in seismology. The two most widely used "families" of

*Corresponding author. *Email addresses:* chenshan05@mails.tsinghua.edu.cn (S. Chen), dhyang@math.tsinghua.edu.cn (D. Yang), xydeng@math.tsinghua.edu.cn (X. Deng)

FD methods are the compact schemes or so-called LWC methods and the staggered-grid schemes. To reduce the computation and memory usage, the high-order compact FD scheme was proposed [1] and widely applied (e.g., [6, 10, 19]). The staggered-grid FD scheme was first developed by Madariaga [12] to model an expanding circular crack in an elastic space. Virieux [17, 18] developed a velocity-stress staggered-grid FD scheme to simulate wave propagating in heterogeneous media. To improve the accuracy and increase the efficiency, Levander [11] developed a fourth-order staggered-grid scheme, and this FD method was later extended to different cases (e.g., [3–5, 13, 16]).

A main reason that the above two kinds FD schemes are so popular is that they can reduce the numerical dispersion resulted from the discretization of wave equations. However, numerical dispersion may still exist when too few samples per wavelength are used [15, 22]. The nearly analytic discrete method (NADM) [25] proposed recently and its improved version (INADM) [21] are much superior with regard to suppressing the numerical dispersion. These methods, based on the truncated Taylor expansion and the local interpolation compensation for the truncated Taylor series, use the wave displacement-, the velocity- and their gradient-fields to reconstruct the wave displacement fields. Thus they can effectively suppress the numerical dispersion, as compared to the compact FD methods [21, 24, 25].

In this paper, we develop an alternate weighted RK method to further suppress the numerical dispersion. In this method, we first use the high-order interpolation approximations to approximate the high-order spatial derivatives and convert the wave equation into a system of ordinary differential equations (ODEs), and then we solve the converted ODEs by using the explicit third-order RK method [7, 14] that is similar to the RK method developed by Yang et al. [20]. Due to the multistage property of the RK method, we introduce a weight to evaluate the displacement and its gradients in every stage, which results in the method called the weighted Runge-Kutta (WRK) method. Since the method not only uses the wave displacement and the particle velocity but also their gradient-fields to reconstruct the wave displacement fields, the WRK method can suppress effectively the numerical dispersion like our previous RK method [20]. But the weight introduced here makes the WRK method much more effective in suppressing the numerical dispersion and in enhancing the stability condition by comparing with the original third-order RK method. However, it should be mentioned that the weight may reduce the accuracy in time.

2 Theory of the WRK method

Third-order Runge-Kutta method

Consider the following differential equation

$$\frac{du}{dt} = L(u). \tag{2.1}$$

If $L(u)$ is a known function at each spatial point (i,j) for the 2D case, then we can solve Eq. (2.1) as an ordinary equation using the following third-order Runge-Kutta method [14]

$$\begin{cases} u^{(1)}=u^n+\dfrac{1}{3}\Delta tL(u^n), \\ u^{(2)}=u^n+\dfrac{2}{3}\Delta tL(u^{(1)}), \\ u^{n+1}=\dfrac{1}{4}u^n+\dfrac{3}{4}u^{(1)}+\dfrac{3}{4}\Delta tL(u^{(2)}). \end{cases} \tag{2.2}$$

Of course, we can also use the fourth-order Runge-Kutta method to solve Eq. (2.1). However, it will obviously increase the computational cost and storage space.

Transforms of wave equations

In 2D anisotropic media, the wave equation describing the elastic wave propagation can be written as

$$\frac{\partial\sigma_{ij}}{\partial x_j}+f_i=\rho\frac{\partial^2u_i}{\partial t^2}, \qquad i=1,2,3, \tag{2.3}$$

where subscript j takes the values of 1 and 3, $\rho=\rho(x,z)$ is the density, u_i and f_i denote the displacement component and the force-source component in the i-th direction, and (σ_{ij}) is the stress tensor.

To demonstrate our method, we transform Eq. (2.3) to the following vector equation [25] using the stress-strain relation

$$\rho\frac{\partial^2U}{\partial t^2}=D\cdot U+f, \tag{2.4}$$

where $U=(u_1,u_2,u_3)^T$, $f=(f_1,f_2,f_3)^T$ and D is the second-order partial differential operator. For example, for the 2D anisotropic case D is defined by

$$D=\frac{\partial}{\partial x}\left(C_1\frac{\partial}{\partial x}+C_2\frac{\partial}{\partial z}\right)+\frac{\partial}{\partial z}\left(C_3\frac{\partial}{\partial x}+C_4\frac{\partial}{\partial z}\right),$$

where

$$C_1=\begin{bmatrix} c_{11} & c_{16} & c_{15} \\ c_{16} & c_{66} & c_{56} \\ c_{15} & c_{56} & c_{55} \end{bmatrix}, C_2=\begin{bmatrix} c_{15} & c_{14} & c_{13} \\ c_{56} & c_{46} & c_{36} \\ c_{55} & c_{45} & c_{35} \end{bmatrix}, C_3=\begin{bmatrix} c_{15} & c_{56} & c_{55} \\ c_{14} & c_{46} & c_{45} \\ c_{13} & c_{36} & c_{35} \end{bmatrix}, C_4=\begin{bmatrix} c_{55} & c_{45} & c_{35} \\ c_{45} & c_{44} & c_{34} \\ c_{35} & c_{34} & c_{33} \end{bmatrix},$$

where $c_{ij}(x,z)$ are the elastic constants.

Let $w_i=\partial u_i/\partial t$, $i=1,2,3$, and $W=(w_1,w_2,w_3)^T$. Then Eq. (2.4) can be rewritten as

$$\begin{cases} \dfrac{\partial W}{\partial t}=\dfrac{1}{\rho}D\cdot U+\dfrac{1}{\rho}f, \\ \dfrac{\partial U}{\partial t}=W. \end{cases} \tag{2.5}$$

For the development of the 2D WRK method, we define the following notations

$$\overline{U}=\left[U,\frac{\partial U}{\partial x},\frac{\partial U}{\partial z}\right]^T, \qquad \overline{W}=\left[W,\frac{\partial W}{\partial x},\frac{\partial W}{\partial z}\right]^T,$$
$$P=\frac{1}{\rho}D\cdot U+\frac{1}{\rho}f, \qquad \overline{P}=\left[P,\frac{\partial P}{\partial x},\frac{\partial P}{\partial z}\right]^T.$$

Then Eq. (2.4) or Eq. (2.5) can be written as follows

$$\begin{cases}\dfrac{\partial \overline{W}}{\partial t}=\overline{P},\\[2ex] \dfrac{\partial \overline{U}}{\partial t}=\overline{W}.\end{cases} \tag{2.6}$$

Obviously, from the definitions of $\overline{U}$, P, $\overline{P}$, and $\overline{W}$, we can see that $\overline{P}$ and $\overline{W}$ in the right-hand side of Eq. (2.6) include the high-order derivatives with respect to spatial coordinate variables x and z.

Weighted Runge-Kutta method

We use the local interpolation method [9, 20, 25] to approximate the high-order spatial derivatives in the right-hand side of Eq. (2.6) by using the values of the wave displacement and its gradients at the grid point (i,j) and its neighboring grid points. These computational formulae of approximating the second- and third-order derivatives are listed in Appendix A. Under this condition, Eq. (2.6) is converted to a system of semi-discrete ODEs with respect to variables $\overline{W}$ and $\overline{U}$, and can be solved by the third-order RK method (formulae (2.2)). In other words, we can apply formulae (2.2) to solve the semi-discrete ODEs (2.6) as follows

$$\overline{W}_{i,j}^{(1)}=\overline{W}_{i,j}^{n}+\frac{\Delta t}{3}\overline{P}_{i,j}^{n}, \tag{2.7a}$$
$$\overline{U}_{i,j}^{(1)}=\overline{U}_{i,j}^{n}+\frac{\Delta t}{3}\overline{W}_{i,j}^{n}, \tag{2.7b}$$
$$\overline{W}_{i,j}^{(2)}=\overline{W}_{i,j}^{n}+\frac{2\Delta t}{3}\overline{P}_{i,j}^{(1)}, \tag{2.7c}$$
$$\overline{U}_{i,j}^{(2)}=\overline{U}_{i,j}^{n}+\frac{2\Delta t}{3}\overline{W}_{i,j}^{(1)}, \tag{2.7d}$$
$$\overline{W}_{i,j}^{n+1}=\frac{1}{4}\overline{W}_{i,j}^{n}+\frac{3}{4}\overline{W}_{i,j}^{(1)}+\frac{3\Delta t}{4}\overline{P}_{i,j}^{(2)}, \tag{2.7e}$$
$$\overline{U}_{i,j}^{n+1}=\frac{1}{4}\overline{U}_{i,j}^{n}+\frac{3}{4}\overline{U}_{i,j}^{(1)}+\frac{3\Delta t}{4}\overline{W}_{i,j}^{(2)}. \tag{2.7f}$$

In order to further suppress the numerical dispersion and relax the stability condition of the third-order RK method, we introduce a weight η in the present work. Note that

the third-order RK algorithm (2.7) above includes totally three stages and the particle-velocity $\overline{W}$ is first computed in every stage. We take the first stage as an example to demonstrate our modification of the RK algorithm (2.7). We notice that the new particle-velocity field $\overline{W}_{i,j}^{(1)}$ has been calculated by formula (2.7a) and we use formula (2.7b) to compute $\overline{U}_{i,j}^{(1)}$. In other words, when we compute $\overline{U}_{i,j}^{(1)}$ using formula (2.7b), we can use not only $\overline{W}_{i,j}^{(n)}$ computed in the former stage but also the new value $\overline{W}_{i,j}^{(1)}$ to compute the displacement field $\overline{U}_{i,j}^{(1)}$. For instance, we can rewrite Eqs. (2.7a) and (2.7b) as follows

$$\overline{W}_{i,j}^{(1)}=\overline{W}_{i,j}^{n}+\frac{\Delta t}{3}\overline{P}_{i,j}^{n}, \tag{2.8a}$$

$$\overline{U}_{i,j}^{(1)}=\overline{U}_{i,j}^{n}+\frac{\Delta t}{3}\left(\eta\overline{W}_{i,j}^{n}+(1-\eta)\overline{W}_{i,j}^{(1)}\right). \tag{2.8b}$$

Similarly, we can rewrite Eqs. (2.7c)-(2.7f) as follows

$$\overline{W}_{i,j}^{(2)}=\overline{W}_{i,j}^{n}+\frac{2\Delta t}{3}\overline{P}_{i,j}^{(1)}, \tag{2.8c}$$

$$\overline{U}_{i,j}^{(2)}=\overline{U}_{i,j}^{n}+\frac{2\Delta t}{3}\left(\eta\overline{W}_{i,j}^{(1)}+(1-\eta)\overline{W}_{i,j}^{(2)}\right), \tag{2.8d}$$

$$\overline{W}_{i,j}^{n+1}=\frac{1}{4}\overline{W}_{i,j}^{n}+\frac{3}{4}\overline{W}_{i,j}^{(1)}+\frac{3\Delta t}{4}\overline{P}_{i,j}^{(2)}, \tag{2.8e}$$

$$\overline{U}_{i,j}^{n+1}=\frac{1}{4}\overline{U}_{i,j}^{n}+\frac{3}{4}\overline{U}_{i,j}^{(1)}+\frac{3\Delta t}{4}\left(\eta\overline{W}_{i,j}^{(2)}+(1-\eta)\overline{W}_{i,j}^{n+1}\right). \tag{2.8f}$$

Eqs. (2.8a)-(2.8f) are called weighted Runge-Kutta (WRK) method. The weight η should be chosen from 0 to 1. Obviously, when $\eta=1$, the method becomes the original third-order RK method. Comparing Eq. (2.7) with Eq. (2.8), we can easily find that the computational cost of the WRK algorithm has slightly increased as compared with the RK method, but the required storage space are the same for the two methods. However, from the numerical tests in the next sections, we will conclude that the WRK method works much better in suppressing the numerical dispersion and in enhancing the stability condition.

3 Stability criteria

In order to keep numerical calculation stable, we must consider how to choose the appropriate time and the space grid sizes, Δt and Δx. As we know, mathematically, the Courant number defined by $\alpha=c\Delta t/\Delta x$ gives the relationship among the velocity c and the two grid sizes, we need to determine the range of α. Following the analyses process presented in Yang et al. [23], after some mathematical derivations, we obtain the stability conditions of the WRK method with the weight η changing from 0 to 1 for 1D and 2D cases (see Appendix B and Fig. 1).

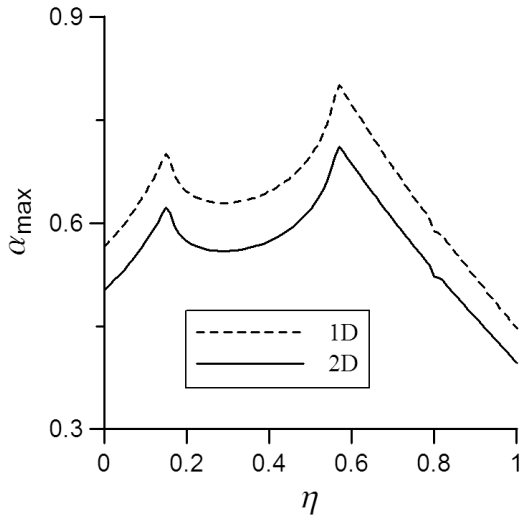

Figure 1: The approximate maximum Courant number $\alpha_{\max}$ changes with the weight η increasing from 0 to 1 for the WRK method for 1D (dashed line) and 2D (solid line) cases.

Fig. 1 shows that the maximum Courant number $\alpha_{\max}$ changes rapidly and reaches its minimal value when $\eta=1$. In other words, the WRK method has more relaxed stability condition than the original third-order RK method can do. In the following sections, we will choose $\eta=0.8$ in computation. Here we give the detailed stability condition of the WRK method with this weight. For the 1D homogeneous case, the stability condition of the WRK method with $\eta=0.8$ is given by

$$\Delta t \leqslant \alpha_{\max}\frac{h}{c} \approx 0.588\frac{h}{c}, \tag{3.1}$$

where h denotes the spatial grid size.

For a 2D homogeneous case, the stability condition of the WRK method with the weight $\eta=0.8$ under the condition $\Delta x=\Delta z=h$ is given by

$$\Delta t \leqslant \alpha_{\max}\frac{h}{c} \approx 0.523\frac{h}{c}. \tag{3.2}$$

For comparison, here we also give the detailed stability condition of the third-order RK method (namely the WRK method with weight $\eta=1$). For the 1D homogeneous case, the stability condition is given by

$$\Delta t \leqslant \alpha_{\max}\frac{h}{c} \approx 0.447\frac{h}{c}, \tag{3.3}$$

and for the 2D homogeneous case, the stability condition is given by

$$\Delta t \leqslant \alpha_{\max}\frac{h}{c} \approx 0.397\frac{h}{c}. \tag{3.4}$$

Comparing the stability conditions (3.1) and (3.2) with (3.3) and (3.4) for 1D and 2D cases, respectively, we can see the stability conditions of the WRK method with weight $\eta=0.8$ are more relaxed than those of the original RK method.

The stability condition for a heterogeneous medium cannot be directly determined but could be approximated by using a local homogeneous case. Our conjecture is that Eqs. (3.1)-(3.4) are approximately correct for a heterogeneous medium if the maximal value of the wave velocity c is used.

4 Error analysis

Theoretical analysis

Using the Taylor series expansion, the errors of $\frac{\partial^{m+l}U}{\partial x^m\partial z^l}$ $(2\leqslant m+l\leqslant 3)$ are $\mathcal{O}(\Delta x^4+\Delta z^4)$ by using the interpolation formulae presented in Appendix A. In other words, the WRK method is a fourth-order accuracy scheme in space. But because only the third-order Runge-Kutta method is used to solve the ODEs (2.6), the temporal derivative error should be $\mathcal{O}(\Delta t^3)$. However, the weight affects the temporal error. For example, when $\eta=0.8$, the temporal accuracy is lower than third-order, which can be seen from the numerical experiments presented in the following subsection.

Numerical errors

Now we investigate the numerical errors of the WRK method. Consider the following 2D initial problem

$$\begin{cases}\dfrac{\partial^2 u}{\partial x^2}+\dfrac{\partial^2 u}{\partial z^2}=\dfrac{1}{\alpha^2}\dfrac{\partial^2 u}{\partial t^2},\\ u(0,x,z)=\cos\left(-\dfrac{2\pi f_0}{\alpha}x\cos\theta_0-\dfrac{2\pi f_0}{\alpha}z\sin\theta_0\right),\\ \dfrac{\partial u(0,x,z)}{\partial t}=-2\pi f_0\sin\left(-\dfrac{2\pi f_0}{\alpha}x\cos\theta_0-\dfrac{2\pi f_0}{\alpha}z\sin\theta_0\right),\end{cases} \tag{4.1}$$

where α is the velocity of the plane wave, θ_0 is the incident angle at time $t=0$ and f_0 is the frequency. The exact solution of this initial problem is

$$u(t,x,z)=\cos\left[2\pi f_0\left(t-\frac{x}{\alpha}\cos\theta_0-\frac{z}{\alpha}\sin\theta_0\right)\right].$$

In the first numerical example, we choose the number of grid points $N=200$, the frequency f_0=30Hz, the wave velocity α=4000m/sec and the angle $\theta_0=\pi/4$. The relative

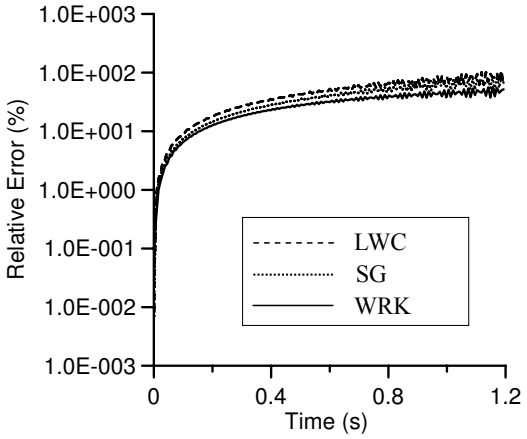

Figure 2: The relative errors of the SG method with accuracy of $\mathcal{O}(\Delta t^2,\Delta x^4)$, the LWC method with accuracy of $\mathcal{O}(\Delta t^4,\Delta x^4)$, and the WRK method measured by E_r (formula (4.2)) are shown in a semilog scale for the 2D initial problem (4.1). The spatial and temporal increments are 30m and 0.5ms, respectively.

error (E_r) for the 2D case is defined by

$$E_r(\%)=\left\{\frac{1}{\sum\limits_{i=1}^{N}\sum\limits_{j=1}^{N}[u(t_n,x_i,z_j)]^2}\sum_{i=1}^{N}\sum_{j=1}^{N}[u_{i,j}^n-u(t_n,x_i,z_j)]^2\right\}^{\frac{1}{2}}\times 100. \tag{4.2}$$

Fig. 2 shows the computational results of the relative error E_r at different times under the condition of $\Delta x=\Delta z$, where three lines of E_r are shown in a semilog scale corresponding to the staggered-grid (SG) method with accuracy of $\mathcal{O}(\Delta t^2,\Delta x^4)$, the LWC method with accuracy of $\mathcal{O}(\Delta t^4,\Delta x^4)$, and the WRK method, respectively. In the calculations, we choose the same time and spatial grid sizes of $\Delta t=5\times 10^{-4}$sec and $\Delta x=\Delta z=30$m. From the figure, we can observe that the error of the WRK method is the smallest among of the three for the chosen computational parameters. And it also numerically illustrates that the WRK method has fourth-order accuracy in space.

Next, we discuss the order of convergence for the WRK method. In this case, we similarly consider the 2D initial problem (4.1), and choose the computational domain as $0<x\leqslant 4$ km, $0<z\leqslant 4$ km and the propagation time $T=1.0$s. The same computational parameters are chosen as those used in the first numerical experiment. In Table 1, we show the numerical errors of the variable u. For the fixed spatial grid size $h=\Delta x=\Delta z$, the error of the numerical solution u_h with respect to the exact solution u is measured in the discrete L^1, L^2 norms

$$E_{L^k}=\|u_h-u\|_{L^k}=\left(h^2\sum_{i=1}^{N}\sum_{j=1}^{N}\left|u_h(x_i,z_j,T)-u(x_i,z_j,T)\right|^k\right)^{\frac{1}{k}},\qquad k=1,2. \tag{4.3}$$

Table 1: Numerical errors and convergence orders of the WRK method with weight $\eta=0.8$.

h	E_{L^1}	E_{L^2}	$\mathcal{O}_{L^1}$	$\mathcal{O}_{L^2}$
5.000E-02	1.959E-02	7.191E-03	—	—
4.000E-02	9.982E-03	3.616E-03	3.022	3.081
3.125E-02	4.969E-03	1.777E-03	2.826	2.858
2.000E-02	1.581E-03	5.569E-04	2.566	2.600

So if we choose two different spatial increments h^{s-1} and h^s for the same computational domain, we can use (4.3) to get two L^k errors $E^{s-1}_{L^k}$ and $E^s_{L^k}$. Then the orders of numerical convergence can be defined by Dumbser et al. [2]

$$\mathcal{O}_{L^k}=\log\left(\frac{E^s_{L^k}}{E^{s-1}_{L^k}}\right)\Big/\log\left(\frac{h^s}{h^{s-1}}\right),\qquad k=1,2. \tag{4.4}$$

Table 1 shows the numerical errors and the convergence orders. In Table 1 the first column shows the spatial increment h, and the following four columns show L^1 and L^2 errors and their corresponding to convergence orders $\mathcal{O}_{L^1}$ and $\mathcal{O}_{L^2}$. From Table 1 we can find that the errors E_{L^1} and E_{L^2} decrease as the spatial grid size h decreases, which implies that the WRK method is convergent.

5 Dispersion analysis

As we all know, the numerical dispersion is the major artifact when we use finite difference schemes to model acoustic and elastic wave-fields. Although the higher-order FD schemes have less dispersion, more grid points in a direction are required for a higher-order scheme. In this section, we investigate the dispersion relation of the WRK method for the 1D case. Its detailed analysis is presented in Appendix C.

Figs. 3-5 plot the dispersion relations of the WRK method and the high-order LWC with accuracies of $\mathcal{O}(\Delta t^4,\Delta x^6)$ and $\mathcal{O}(\Delta t^4,\Delta x^8)$ for the 1D acoustic wave equation, corresponding to different values of the Courant number $\alpha(=c\Delta t/\Delta x)$. From Figs. 3-5 we can observe that the dispersion error of the WRK method with the weight 0.8 is the smallest among these three schemes for the same Courant number. Fig. 3 also shows that the numerical velocity of the WRK method gradually approximates the exact wave velocity as the Courant number α increases. When α is 0.5, the numerical velocity is closest to the exact velocity c. It suggests that the WRK method has the smallest numerical dispersion when the Courant number is about 0.5 for the 1D case.

In the following, we further investigate the numerical dispersion of the WRK method by modeling waveforms. For this case, we consider the following 2D acoustic wave equation in a homogenous medium

$$\frac{\partial^2 u}{\partial t^2}=\frac{\mu}{\rho}\left(\frac{\partial^2 u}{\partial x^2}+\frac{\partial^2 u}{\partial z^2}\right)+f, \tag{5.1}$$

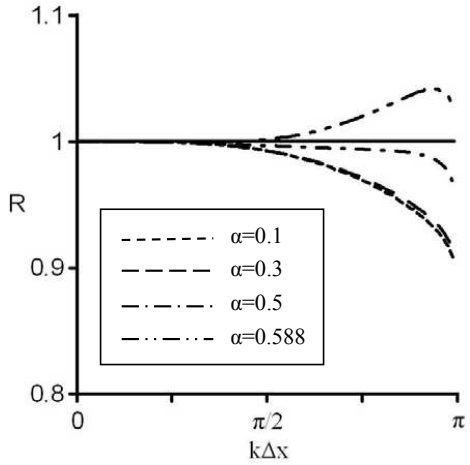

Figure 3: The ratio R of the numerical velocity to the phase velocity versus wave-number $k\Delta x$ for the WRK method with weight $\eta=0.8$ for different Courant numbers $\alpha=c\Delta t/\Delta x$, where four lines correspond to $\alpha=$0.1, 0.3, 0.5 and 0.588, respectively.

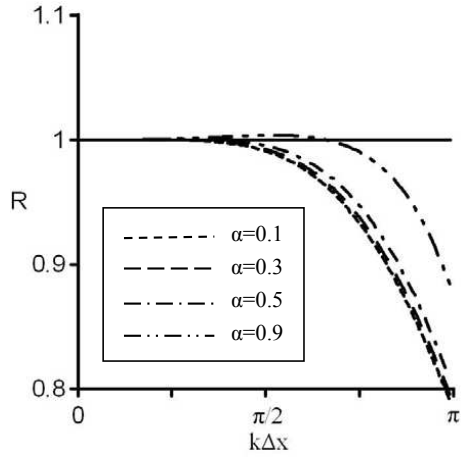

Figure 4: The ratio R of the numerical velocity to the phase velocity versus wave-number $k\Delta x$ for the sixth-order LWC method for different Courant numbers $\alpha=c\Delta t/\Delta x$, where four lines correspond to $\alpha=$0.1, 0.3, 0.5 and 0.9, respectively.

where μ is the Lamé parameter, and ρ is density. In this numerical experiment, we choose $\mu=72$GPa and $\rho=2.0\text{g/cm}^3$. The source, which is located at the center of the computational domain, is a Ricker wavelet

$$f=-5.76f_0^2[1-16(0.6f_0t-1)^2]\exp[-8(0.6f_0t-1)^2], \tag{5.2}$$

where f_0 denotes the peak frequency. The computational domain is $0\leq x\leq 15$ km, $0\leq z\leq 15$ km and the receiver is at R(7.5 km, 3.0 km).

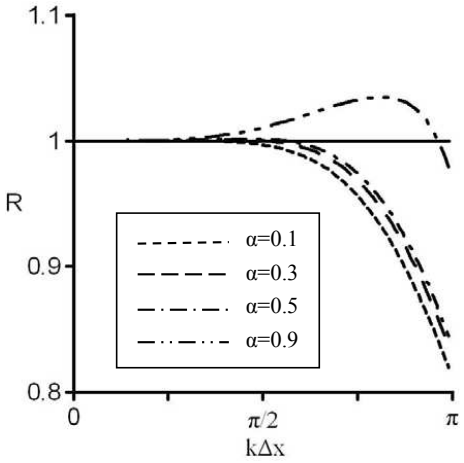

Figure 5: The ratio R of the numerical velocity to the phase velocity versus wave-number $k\Delta x$ for the eighth-order LWC method for different Courant numbers $\alpha = c\Delta t/\Delta x$, where four lines correspond to α =0.1, 0.3, 0.5 and 0.9, respectively.

Fig. 6 show the waveforms at the receiver R from $t = 0.4$sec to $t = 1.2$sec on the spatial grid $\Delta x = \Delta z = 50$m, computed using the fourth-order LWC, the eighth-order LWC, the third-order RK, and our present WRK method, respectively. In this experiment, we choose the time increment $\Delta t = 2.3\times 10^{-3}$s and the peak frequency $f_0 = 30$Hz. We can observe that the waveforms in Figs. 6(b), 6(c) and 6(d) are almost identical, whereas the fourth-order LWC method suffers from serious numerical dispersion (see Fig. 6(a)).

Fig. 7 also show the waveforms at receiver R on the same temporal and spatial increments computed by these four methods. But the peak frequency $f_0 = 60$Hz is chosen here. From Figs. 7(a) and 7(b) we can see that even the high-order LWC methods (eighth-order) suffer from serious numerical dispersions. However, Figs. 7(c) and 7(d), generated by the RK and the WRK methods, show clear waveforms and they do not show much numerical dispersion for the higher frequency. Especially Fig. 7(d) computed by the WRK method shows almost no visible numerical dispersion in such a high frequency case. It demonstrates that the WRK is more efficient than the high-order LWC methods such as the fourth-order and eighth-order methods in suppressing the numerical dispersion and improves the third-order RK method.

To further investigate the effect of the spatial increment on the numerical dispersion, we similarly define the spatial sampling number per minimum wavelength (Dablain [1]) as follows

$$G = \frac{v_{\min}}{f_0 \cdot \Delta x}, \tag{5.3}$$

where $v_{\min}$ denotes the minimum acoustic wave-velocity and f_0 is the peak frequency.

Using the definition (5.3), we have $G = 4$ for the case of $\Delta x = \Delta z = 50$m in generating Fig. 6 and $G = 2$ for generating Fig. 7 which show serious numerical dispersion for these high-order LWC methods while the WRK has no visible numerical dispersion (see

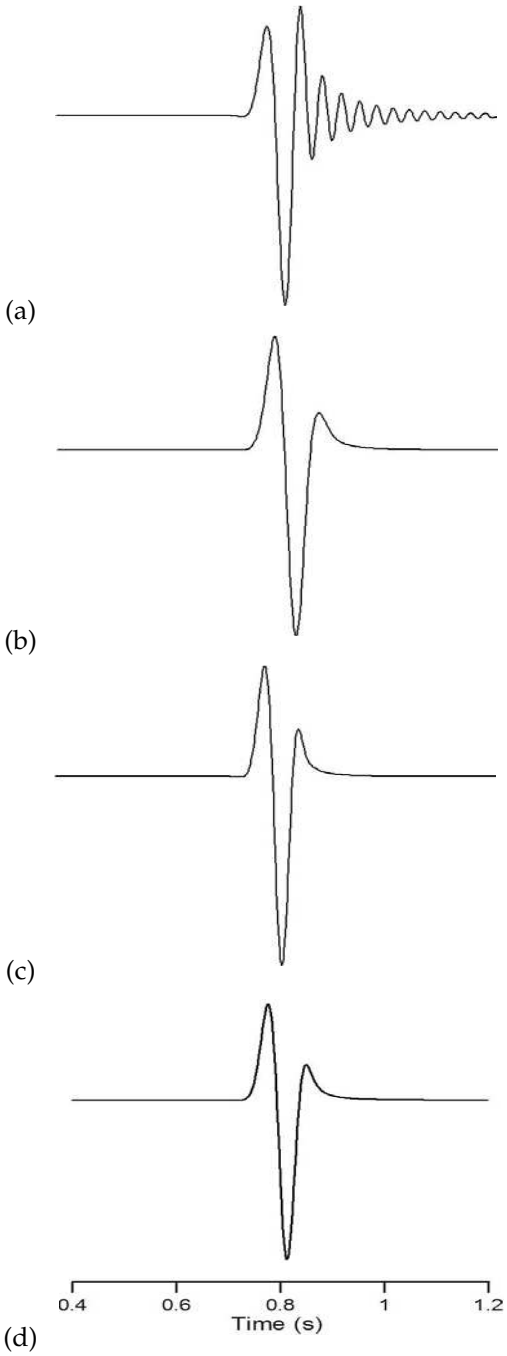

Figure 6: The waveforms generated by the fourth-order LWC method (a), and the eighth-order LWC method (b), the RK method (c), the WRK method (d) for the 2D homogeneous case and the Ricker wavelet with the peak frequency $f_0 = 30$Hz.

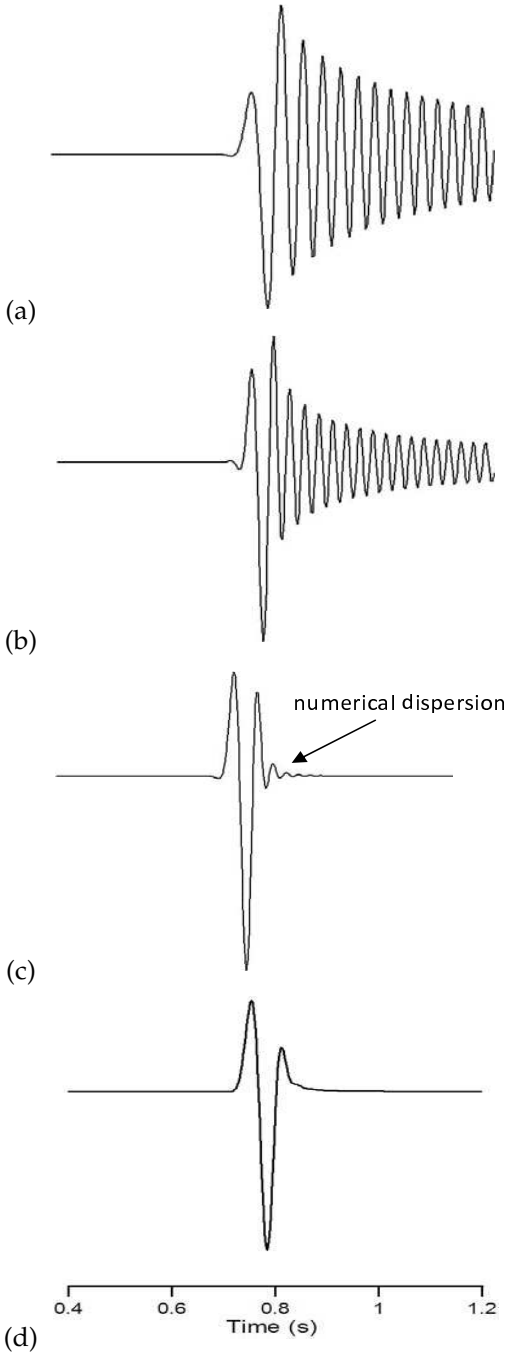

Figure 7: The waveforms generated by the fourth-order LWC method (a), and the eighth-order LWC method (b), the RK method (c), the WRK method (d) for the 2D homogeneous case and the Ricker wavelet with the peak frequency $f_0 = 60$Hz.

Fig. 7(d)). It indicates that the present method can use only 2 grid points per minimum acoustic wavelength for nondispersive propagation while the fourth-order LWC method should use more than 4. It implies that the WRK can increase the computational efficiency of wave-field simulation significantly, especially for high dimensional problems. We will confirm this conclusion in the numerical experiments below. Meanwhile, we can see small numerical dispersion around the wave from peak in Fig. 7(c) computed by using the third-order RK method, whereas Fig. 7(d) generated by the WRK shows almost no visible numerical dispersion. It illustrates that the weighted RK method can further suppress the numerical dispersion as compared with the original RK method.

6 Wave-field simulation

In this section, we present more computational results and investigate the computational efficiency of the WRK method for seismic waves propagating in the 2D homogeneous transversely isotropic (TI) medium and the 2D heterogeneous isotropic medium.

2D homogeneous TI case

For this case, we consider the following elastic-wave equations in a 2D homogeneous TI medium:

$$\begin{cases} \rho\dfrac{\partial^2 u}{\partial t^2}=c_{11}\dfrac{\partial^2 u}{\partial x^2}+(c_{13}+c_{44})\dfrac{\partial^2 w}{\partial x\partial z}+c_{44}\dfrac{\partial^2 u}{\partial z^2}+f_1, \\ \rho\dfrac{\partial^2 w}{\partial t^2}=(c_{13}+c_{44})\dfrac{\partial^2 u}{\partial x\partial z}+c_{44}\dfrac{\partial^2 w}{\partial x^2}+c_{33}\dfrac{\partial^2 w}{\partial z^2}+f_2, \end{cases} \tag{6.1}$$

where u and w denote the displacement components in the x- and z-directions, respectively. c_{11}, c_{13}, c_{33}, and c_{44} are elastic constants, ρ is the medium density, f_1 and f_2 are the force source components in the x- and z-directions.

In this experiment, we choose $c_{11}=45$, $c_{13}=9.6$, $c_{33}=37.5$, $c_{44}=12$ (GPa), and $\rho=1.0\text{g/cm}^3$. The number of grid points is 301×301, the spatial grid increments are $\Delta x=\Delta z=50$m, and the time increment is $\Delta t=3.5\times10^{-3}$s. The source, which is located at the center of the computation domain, is a Ricker wavelet with dominant frequency of $f_0=30$Hz. The time variation of the source function is the same as that of the 2D homogeneous acoustic case in the section for dispersion analysis above.

Figs. 8 and 9 show the x- and z-component snapshots at $t=1.0$sec on a coarse grid ($\Delta x=\Delta z=50$m), generated respectively by the WRK method and the fourth-order LWC method [1], whereas Fig. 10 shows the x- and z-component snapshots at $t=1.0$sec under the same Courant number and on a fine grid ($\Delta x=\Delta z=15$m) chosen for eliminating the numerical dispersion, generated by the fourth-order LWC method. From Figs. 8 and 9 we can see that the wavefronts of seismic waves simulated by these two methods are basically identical, though the computational cost of the WRK method is more expensive than the fourth-order LWC method for the same number of grid points because more

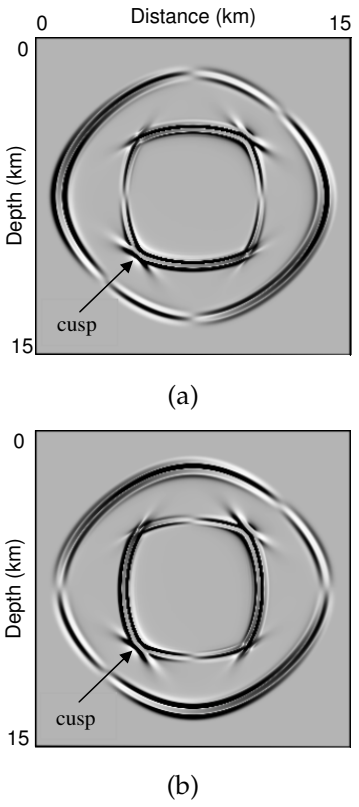

Figure 8: Snapshots of seismic wave fields at time 1.6s on the coarse grid $\Delta x=\Delta z=50$m, generated by the WRK method in the TI medium. (a) u component; (b) w component.

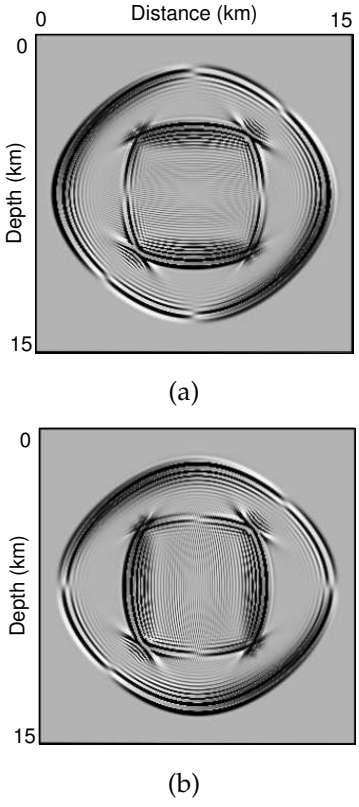

Figure 9: Snapshots of seismic wave fields at time 1.6s on the coarse grid $\Delta x=\Delta z=50$m, generated by the fourth-order LWC method in the TI medium. (a) u component; (b) w component.

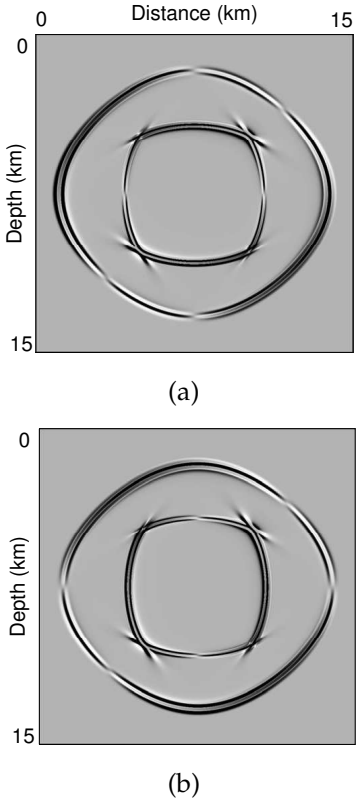

Figure 10: Snapshots of seismic wave fields at time 1.6s on the fine grid $\Delta x=\Delta z=15$m, generated by the fourth-order LWC method in the TI medium. (a) u component; (b) w component.

variables including displacement, particle-velocity, and their gradients are simultaneously computed in this WRK method. However, the snapshots generated by the WRK method have much less numerical dispersion even though the spatial grid size is 50m, whereas the fourth-order LWC method suffers from serious numerical dispersions. It suggests that the WRK method can be used to simulate large-scale models with coarse grids. Moreover, we can clearly see the cusps and the anisotropy of velocity of wave propagating from Fig. 8.

Comparison between Fig. 8 and Fig. 10 demonstrates that our present method can provide the same accuracy as the fourth-order LWC method on a fine grid under the same Courant number. But their computational costs are quite different. It took the WRK method about 1.9 min to generate Fig. 8, whereas it took the fourth-order LWC method about 22.2 min to generate Fig. 10. It suggests that the computational efficiency of the WRK is roughly 11.7 times of that of the fourth-order LWC method on a fine grid to

achieve the same accuracy with no visible wave-field dispersion. Note that these numerical experiments are performed on a 2-core Pentium 4 computer with 1G memory.

2D heterogeneous case

In the final experiment, we choose the following 2D heterogeneous wave equation

$$\frac{\partial^2 u}{\partial t^2}=\frac{1}{\rho(x,z)}\left[\frac{\partial}{\partial x}\left(\mu(x,z)\frac{\partial u}{\partial x}\right)+\frac{\partial}{\partial z}\left(\mu(x,z)\frac{\partial u}{\partial z}\right)\right]+\frac{f}{\rho(x,z)}, \tag{6.2}$$

where $\rho(x,z)$ is the density, $\mu(x,z)$ is the elastic parameter, f is the source function with the same time variation as that of the 2D homogeneous case. We choose the model of three-layer media, which is shown in Fig. 11. The computational domain is $0\leq x\leq 20$ km, $0\leq z\leq 16$ km. The first interface is governed by the following subsection function

$$z=\begin{cases} 6, & 0\leqslant x<3; \\ x+3, & 3\leqslant x<5; \\ 8, & 5\leqslant x<12; \\ 12-\sqrt{25-(x-15)^2}, & 12\leqslant x<18; \\ 8, & 18\leqslant x\leqslant 20, \end{cases} \tag{6.3}$$

and the second interface is horizontally straight line at z=10km. The medium parameters are chosen by $\mu_1(x,z)=36.8$GPa, $\rho_1(x,z)=2.3\text{g/cm}^3$, and $\mu_2(x,z)=8.0$GPa, $\rho_2(x,z)=2.0\text{g/cm}^3$, and $\mu_3(x,z)=36.8$GPa, $\rho_3(x,z)=2.3\text{g/cm}^3$ in the three layers, respectively, resulting in the velocity contrast between adjacent layers reaches twice. We choose the spatial increments $\Delta x=\Delta z=40$m, and the number of grid points 501×401. The source is an explosive source that is at coordinate (x_s,z_s) =(10km, 0.04km) and has a Ricker wavelet with a peak frequency being $f_0=20$Hz. In this numerical experiment, the 2-times absorbing boundary condition suggested by Yang et al. [22] is used to absorb the reflected waves from the artificial boundaries.

Figs. 12 and 13 show the snapshots at t=2.8sec and t=3.8sec on the spatial increments of $\Delta x=\Delta z=40$m, generated by the WRK method and the fourth-order LWC method, respectively. In these two figures we can see that the wavefronts of transmitted waves and reflected waves from the first and second interface simulated by these two methods are basically identical. However, the LWC method suffers from serious numerical dispersion, whereas the WRK method gives much better wave-field that shows clearly numerous phases such as direct qP-wave, direct qS-wave, and their reflected, transmitted, converted phases, and so on (Fig. 12). Fig. 14 shows the synthetic seismogram generated by the WRK method. In this figure, the waveforms of the reflected waves are clear and there is no visible numerical dispersion. These results imply that the WRK method is effective to model the large-scale seismic wave-fields in heterogeneous cases even though the velocity contrast between adjacent layers is twice.

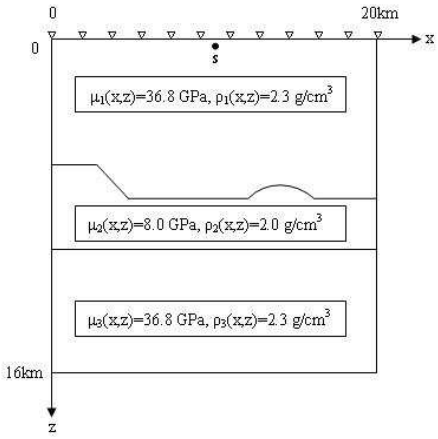

Figure 11: Two-dimensional medium model with two inner interfaces, s denotes the explosive source, which is located at (x_s,z_s)=(10km, 0.04km).

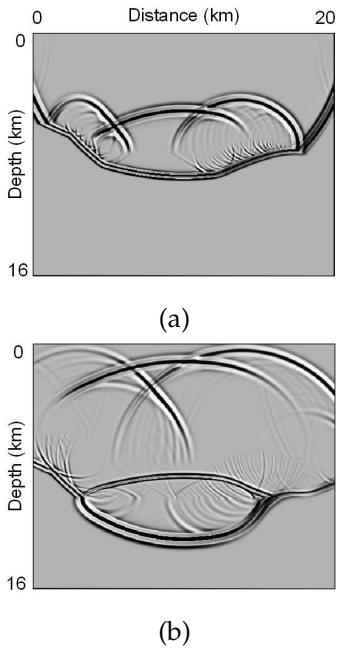

Figure 12: Snapshots of seismic wave fields at time 2.8s (a) and 3.8s (b), generated by the WRK method for the 2D model shown in Fig. 11.

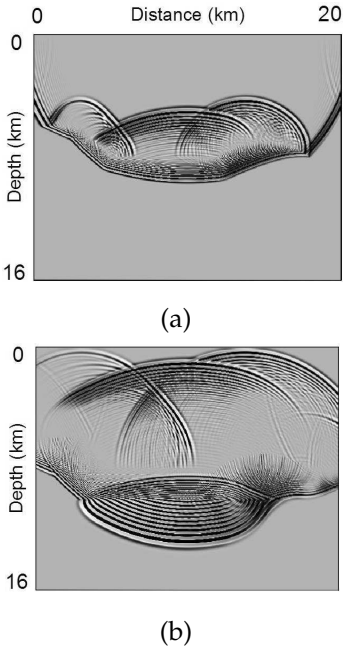

Figure 13: Snapshots of seismic wave fields at time t =2.8s (a) and t=3.8s (b), generated by the fourth-order LWC method for the 2D model shown in Fig. 11.

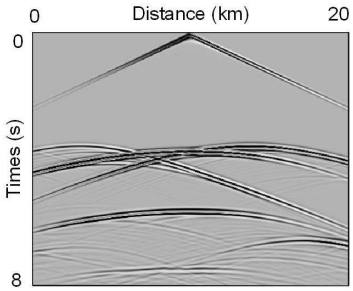

Figure 14: The synthetic seismogram on the surface, generated by the WRK method for the 2D model shown in Fig. 11.

7 Discussion and conclusions

In this paper, we present a weighted method called WRK method which extends the conventional third-order RK method [7, 14]. In determining the high-order spatial deriva-

tives, the WRK method not only uses the values of the displacement U and the particle-velocity W at the grid point and its neighboring grid points (see Eqs. (A.1)-(A.7)), it also uses the values of the gradients of U and W, which follows the fourth-order RK method suggested by Yang et al. [20]. Based on such a structure, the WRK method retains more wave-field information included in the displacement function, the particle-velocity, and their gradients. As a result, the WRK method can effectively suppress the numerical dispersion caused by discretizing the wave equations when too-coarse grids are used or models have large velocity contrast in adjacent layers, and has higher spatial accuracy though it only uses a local difference-operator of three grid points in a spatial direction. Numerical results illustrate that the weighted method can still effectively suppress the numerical dispersion even though the number of grid points per minimum wavelength is only 2. It implies that the WRK has faster computational speed.

In addition, the introduction of the weight factor is another important skill used in this WRK method. It has almost no additional computational cost and storage. Secondly, through introducing the weight, the WRK method has two remarkable improvements: (1) the WRK further improves the RK method in suppressing the numerical dispersion; (2) the stability condition of the WRK method is also relaxed as compared to the original RK method. Both of these two properties imply that for the same problem, the WRK method can use coarser time and spatial grid size as compared to the original RK method, which makes the WRK method to be computationally more efficient and save the storage space. Numerical tests for wave-field snapshots and synthetic seismograms in various media have demonstrated that the WRK method may have more attractive applications to the seismic wave propagation problems, seismic migration based on the wave equations, and the seismic tomography.

Acknowledgments

We thank two anonymous reviewers for their detailed comments and helpful suggestions that greatly contributed to improving the manuscript. Special thanks go to Dr. Faqi Liu for his help that substantially improves the presentation of the article. This work was supported by the National Science Fund for Distinguished Young Scholars of China (Grant No. 40725012).

A Evaluation of high-order derivatives

To get the high-order derivatives of the displacement, following Konddoh [9] and Yang et al. [25], we can obtain the approximation formulae by using the local interpolation method, which have similar expressions as in [21]. For convenience, we present the ap-

proximation formulae as follows

$$\partial_{2x}V_{i,j}^n=\frac{2}{\Delta x^2}\delta_x^2V_{i,j}^n-\frac{1}{2\Delta x}\left(E_x^1-E_x^{-1}\right)\partial_xV_{i,j}^n, \tag{A.1}$$

$$\partial_{xz}V_{i,j}^n=\frac{1}{2\Delta x}\left(E_x^1-E_x^{-1}\right)\partial_zV_{i,j}^n+\frac{1}{2\Delta z}\left(E_z^1-E_z^{-1}\right)\partial_xV_{i,j}^n -\frac{1}{4\Delta x\Delta z}\left(E_x^1E_z^1-E_x^1E_z^{-1}-E_x^{-1}E_z^1+E_x^{-1}E_z^{-1}\right)V_{i,j}^n, \tag{A.2}$$

$$\partial_{2z}V_{i,j}^n=\frac{2}{\Delta z^2}\delta_z^2V_{i,j}^n-\frac{1}{2\Delta z}\left(E_z^1-E_z^{-1}\right)\partial_zV_{i,j}^n, \tag{A.3}$$

$$\partial_{3x}V_{i,j}^n=\frac{15}{2\Delta x^3}\left(E_x^1-E_x^{-1}\right)V_{i,j}^n-\frac{3}{2\Delta x^2}\left(E_x^1+8I+E_x^{-1}\right)\partial_xV_{i,j}^n, \tag{A.4}$$

$$\partial_{3z}V_{i,j}^n=\frac{15}{2\Delta z^3}\left(E_z^1-E_z^{-1}\right)V_{i,j}^n-\frac{3}{2\Delta z^2}\left(E_z^1+8I+E_z^{-1}\right)\partial_zV_{i,j}^n, \tag{A.5}$$

$$\partial_{2xz}V_{i,j}^n=\frac{1}{4\Delta x^2\Delta z}\left(5E_x^1E_z^1-5E_x^{-1}E_z^{-1}+E_x^1E_z^{-1}-E_x^{-1}E_z^1-4E_z^1+4E_z^{-1}-6E_x^1+6E_x^{-1}\right)V_{i,j}^n +\frac{1}{2\Delta x\Delta z}\left(-E_x^1E_z^1-E_x^{-1}E_z^{-1}+E_x^1+E_x^{-1}-2\delta_z^2\right)\partial_xV_{i,j}^n+\frac{1}{\Delta x^2}\delta_x^2(\partial_zV_{i,j}^n), \tag{A.6}$$

$$\partial_{x2z}V_{i,j}^n=\frac{1}{4\Delta x^2\Delta z}\left(5E_x^1E_z^1-5E_x^{-1}E_z^{-1}-E_x^1E_z^{-1}+E_x^{-1}E_z^1-4E_x^1+4E_x^{-1}-6E_z^1+6E_z^{-1}\right)V_{i,j}^n +\frac{1}{2\Delta x\Delta z}\left(-E_x^1E_z^1-E_x^{-1}E_z^{-1}+E_z^1+E_z^{-1}-2\delta_x^2\right)\partial_zV_{i,j}^n+\frac{1}{\Delta z^2}\delta_z^2(\partial_xV_{i,j}^n), \tag{A.7}$$

where

$$\delta_x^2V_{i,j}^n=V_{i+1,j}^n-2V_{i,j}^n+V_{i-1,j}^n,\quad E_x^1V_{i,j}^n=V_{i+1,j}^n,\quad E_x^{-1}V_{i,j}^n=V_{i-1,j}^n.$$

Notice that the vector V is defined by $V=(U,W)^T$, where U and W are the displacement and the particle-velocity, respectively. The notations δ_z^2 and E_z can be similarly defined. Δx and Δz are the spatial increments in the x- and z-axis directions. And $V_{i,j}^n$, $\partial_xV_{i,j}^n$, $\partial_zV_{i,j}^n$, and $\partial_{mxkz}V_{i,j}^n$ denote $V(i\Delta x,j\Delta z,n\Delta t)$, $\frac{\partial}{\partial x}V(i\Delta x,j\Delta z,n\Delta t)$, $\frac{\partial}{\partial z}V(i\Delta x,j\Delta z,n\Delta t)$, and $\left(\partial^{m+k}V/\partial x^m\partial z^k\right)_{i,j}^n$, respectively.

B Derivation of stability criteria

We use the Fourier method to obtain the stability conditions of WRK method. Firstly, we consider the scalar wave equation in a homogeneous medium for the 1D case. Substituting the harmonic solution

$$\overline{V}_j^n=\begin{pmatrix}u^n\\ w^n\\ u_x^n\\ w_x^n\end{pmatrix}\exp(i(kjh)) \tag{B.1}$$

into the WRK method, we can obtain the following equation

$$\left(u^{n+1},w^{n+1},u_x^{n+1},w_x^{n+1}\right)^T=G(u^n,w^n,u_x^n,w_x^n)^T, \tag{B.2}$$

where $w=\partial u/\partial t$ and the amplification matrix G is

$$G=\begin{bmatrix} g_{11} & g_{12} & g_{13} & g_{14} \\ g_{21} & g_{22} & g_{23} & g_{24} \\ g_{31} & g_{32} & g_{33} & g_{34} \\ g_{41} & g_{42} & g_{43} & g_{44} \end{bmatrix}, \tag{B.3}$$

with

$$\begin{aligned}
g_{11}=&1-\frac{2}{3}(5-2\eta)\alpha^2(1-\cos\theta)+\frac{1}{144}(18-23\eta+5\eta^2)\alpha^4(63-64\cos\theta+\cos2\theta)\\
&-\frac{1}{144}(1-\eta)^3\alpha^6(1240-1035\cos\theta-216\cos2\theta+11\cos3\theta),\\
g_{12}=&\frac{ih}{144}\Big[-12(5-2\eta)\alpha^2\sin\theta+(18-23\eta+5\eta^2)\alpha^4(4\sin\theta-\sin2\theta)\\
&-(1-\eta)^3\alpha^6(444\sin\theta+8\sin2\theta-2\sin3\theta)\Big],\\
g_{13}=&\frac{\tau}{24}\Big[24-4(9-5\eta)\alpha^2(1-\cos\theta)+(1-\eta)^2\alpha^4(63-64\cos\theta+\cos2\theta)\Big],\\
g_{14}=&\frac{i\tau h}{24}\Big[(9-5\eta)\alpha^2\sin\theta-(1-\eta)^2\alpha^4(32\sin\theta-\sin2\theta)\Big],\\
g_{21}=&\frac{5i}{48h}\Big[12(5-2\eta)\alpha^2\sin\theta-(18-23\eta+5\eta^2)\alpha^4(4\sin\theta-\sin2\theta)\\
&+(1-\eta)^3\alpha^6(444\sin\theta+8\sin2\theta-2\sin3\theta)\Big],\\
g_{22}=&1-(5-2\eta)\alpha^2\left(2+\frac{1}{2}\cos\theta\right)+(18-23\eta+5\eta^2)\alpha^4\left(\frac{13}{6}+\cos\theta-\frac{1}{24}\cos2\theta\right)\\
&-(1-\eta)^3\alpha^6\left(\frac{175}{3}+\frac{1765}{48}\cos\theta-\frac{4}{3}\cos2\theta-\cos3\theta\right),\\
g_{23}=&\frac{5i\tau}{8h}\Big[(9-5\eta)\alpha^2\sin\theta-(1-\eta)^2\alpha^4(32\sin\theta-\sin2\theta)\Big],\\
g_{24}=&\tau-\frac{\tau}{8}\Big[(9-5\eta)\alpha^2(4+\cos\theta)+(1-\eta)^2\alpha^4(208+48\cos\theta-2\cos2\theta)\Big],\\
g_{31}=&\frac{1-\cos\theta}{54\tau}\Big[-216\alpha^2+(2-\eta)\alpha^4(279-9\cos\theta)-(1-\eta)^2\alpha^6(717+194\cos\theta-11\cos2\theta)\Big],\\
g_{32}=&\frac{ih}{108\tau}\Big[-108\alpha^2\sin\theta+(2-\eta)\,\alpha^4(288\sin\theta+9\sin2\theta)\\
&-(1-\eta)^2\alpha^6(888\sin\theta-8\sin2\theta+2\sin3\theta)\Big],\\
g_{33}=&1-2\alpha^2(1-\cos\theta)+\frac{1}{18}(1-\eta)\alpha^4(63-64\cos\theta+\cos2\theta),\\
g_{34}=&\frac{ih}{18}\Big[-9\alpha^2\sin\theta+(1-\eta)\alpha^4(32\sin\theta-\sin2\theta)\Big],\\
g_{41}=&\frac{5i}{36h\tau}\Big[108\alpha^2\sin\theta-(2-\eta)\,\alpha^4(288\sin\theta+9\sin2\theta)\\
&+(1-\eta)^2\alpha^6(888\sin\theta-8\sin2\theta+2\sin3\theta)\Big],
\end{aligned}$$

$$g_{42}=\frac{1}{36\tau}\Big[-\alpha^2(432+108\cos\theta)+(2-\eta)\alpha^4(8+432\cos\theta-18\cos2\theta)$$
$$-(1-\eta)^2\alpha^6(2800+1765\cos\theta-64\cos2\theta+\cos3\theta)\Big],$$
$$g_{43}=\frac{5i}{6h}\Big[-9\alpha^2\sin\theta+(1-\eta)\alpha^4(32\sin\theta-\sin2\theta)\Big],$$
$$g_{44}=1-3\alpha^2\left(2+\frac{1}{2}\cos\theta\right)+\frac{1}{3}(1-\eta)\alpha^4(52+24\cos\theta-\cos2\theta),$$

where $\theta=kh$, $h=\Delta x$, and $\tau=\Delta t$ is the time step, and the Courant number [1,15] is defined by $\alpha=c\tau/h$. From the matrix G, we can obtain numerically the stability condition with different weights η $(0\leq\eta\leq1)$ by solving the eigenvalue problem $|\lambda(G)|\leqslant1$, for any $\theta\in[-\pi,\pi]$. As an example, we give the following stability condition numerically when the weight $\eta=0.8$:

$$\alpha\leqslant\alpha_{\max}\approx0.588, \tag{B.4a}$$

or

$$\Delta t\leqslant\alpha_{\max}\frac{h}{c}\approx0.588\frac{h}{c}, \tag{B.4b}$$

where $\alpha_{\max}$ denotes the maximum Courant number that keeps the numerical calculation stable. We also give a plot of how $\alpha_{\max}$ changes with the weight η, see the dashed line in Fig. 1.

Following the same steps as discussed in the 1D case, we can obtain the stability condition of the WRK method with different weights η $(0\leq\eta\leq1)$ for the 2D homogeneous case. The solid line in Fig. 1 shows how $\alpha_{\max}$ changes with the weight η. Here we still give the stability condition of the WRK method for the 2D case when the weight $\eta=0.8$:

$$\alpha\leqslant\alpha_{\max}\approx0.523. \tag{B.5}$$

C Derivation of the dispersion relation

To investigate and optimize the dispersion error, we derive the dispersion relation of the WRK method. For this, following the analysis methods presented in Dablain [1] and Yang et al. [23], we consider the harmonic solution of Eq. (2.6) for the 1D case and substitute the solution

$$\overline{V}_j^n=\begin{pmatrix}u_0\\ w_0\\ (u_0)_x\\ (w_0)_x\end{pmatrix}\exp[i(\omega_{num}n\Delta t+kjh)] \tag{C.1}$$

into Eqs. (2.8a)-(2.8f), where k is the wave number, then we can obtain the dispersion equation as follows:

$$\det(M)=0. \tag{C.2}$$

Due to the complexity of elements of the amplification matrix M, we omit the detail expressions of the matrix M here.

Using the dispersion relation (C.2), we obtain the ratio of the numerical velocity c_{num} to the phase velocity c as follows:

$$R=\frac{c_{num}}{c}=\frac{\omega_{num}\Delta t}{\alpha\theta}=\frac{\gamma}{\alpha\theta}, \tag{C.3}$$

where α is the Courant number, $\theta=kh$, $h=\Delta x$, $\gamma=\omega_{num}\Delta t$ and γ satisfies the dispersion equation (C.2).

References

[1] M. A. Dablain, The application of high-order differencing to the scalar wave equation, Geophysics, 51 (1986), 54-66.

[2] M. Dumbser, M. Käser and E. F. Toro, An arbitrary high-order discontinuous Galerkin method for elastic waves on unstructured meshes - V. Local time stepping and p-adaptivity, Geophys. J. Int., 171 (2007), 695-717.

[3] E. L. Faria and P. L. Stoffa, Finite-difference modeling in transversely isotropic media, Geophysics, 59 (1994), 282-289.

[4] B. Fornberg, High-order finite differences and pseudo-spectral method on staggered grids, SIAM J. Numer. Anal., 27 (1990), 904-918.

[5] R. W. Graves, Simulating seismic wave propagation in 3D elastic media using staggered-grid finite differences, Bull. Seism. Soc. Am., 86 (1996), 1091-1106.

[6] J. Igel and M. Weber, SH-wave propagation in the whole mantle using high-order finite differences, Geophys. Res. Lett., 22 (1995), 731-734.

[7] G. S. Jiang and C. W. Shu, Efficient implementation of Weighted ENO schemes, J. Comput. Phys., 126 (1996), 202-228.

[8] K. Kelly, R. Ward, S. Treitel and R. Alford, Synthetic seismograms: A finite-difference approach, Geophysics, 41 (1976), 2-27.

[9] Y. Konddoh, Y. Hosaka and K. Ishii, Kernel optimum nearly analytical discretization algorithm applied to parabolic and hyperbolic equations, Computers Math. Appl., 27 (1994), 59-90.

[10] S. K. Lele, Compact finite difference scheme with spectral-like resolution, J. Comput. Phys., 103 (1992), 16-42.

[11] A. R. Levander, Fourth-order finite-difference P-SV seismograms, Geophysics, 53 (1988), 1425-1436.

[12] R. Madariaga, Dynamics of an expanding circular fault, Bull. Seism. Soc. Am., 67 (1976), 1529-1540.

[13] P. Moczo, J. Kristek, V. Vavryčuk, R. J. Archuleta and L. Halada, 3D heterogeneous staggered-grid finite-difference modeling of seismic motion with volume harmonic and arithmetic averaging of elastic moduli and densities, Bull. Seism. Soc. Am., 92 (2002), 3042-3066.

[14] J. X. Qiu, T. G. L and B. C. Khoo, Simulations of compressible two-medium flow by Runge-Kutta discontinuous Galerkin methods with the ghost fluid method, Commun. Computs. Phys., 3 (2008), 479-504.

[15] A. Sei and W. Symes, Dispersion analysis of numerical wave propagation and its computational consequences, J. Sci. Comput., 10 (1994), 1-27.
[16] K. Shiraishi and T. Matsuoka, Wave propagation simulation using the CIP method of characteristic equations, Commun. Comput. Phys., 3 (2008), 121-135.
[17] J. Virieux, SH-wave propagation in heterogeneous media: Velocity-stress finite-difference method, Geophysics, 49 (1984), 1933-1957.
[18] J. Virieux, P-SV wave propagation in heterogeneous media: Velocity-stress finite-difference method, Geophysics, 51 (1986), 889-901.
[19] S. Q. Wang, D. H. Yang and K. D. Yang, Compact finite difference scheme for elastic equations, J. Tsinghua Univ. (Sci. & Tech.), 42 (2002), 1128-1131, (in Chinese).
[20] D. H. Yang, S. Chen and J. Z. Li, A Runge-Kutta method using high-order interpolation approximation for solving 2D acoustic and elastic wave equations, J. Seismic Exploration, 16 (2007), 331-353.
[21] D. H. Yang, E. R. Liu, G. J. Song and N. Wang, Elastic wave modelling method based on the displacement-velocity fields: An improving nearly-analytic discrete approximation, J. Seismology, 13 (2009), 209-217.
[22] D. H. Yang, E. Liu, Z. J. Zhang and J. Teng, Finite-difference modelling in two-dimensional anisotropic media using a flux-corrected transport technique, Geophys. J. Int., 148 (2002), 320-328.
[23] D. H. Yang, J. M. Peng, M. Lu and T. Terlaky, Optimal nearly analytic discrete approximation to the scalar wave equation, Bull. Seism. Soc. Am., 96 (2006), 1114-1130.
[24] D. H. Yang, J. M. Peng, M. Lu and T. Terlaky, A nearly analytical discrete method for wavefield simulations in 2D porous media, Commun. Comput. Phys., 1 (2006), 530-549.
[25] D. H. Yang, J. W. Teng, Z. J. Zhang and E. Liu, A nearly-analytic discrete method for acoustic and elastic wave equations in anisotropic media, Bull. Seism. Soc. Am., 93 (2003), 882-890.